To Delay or Not to Delay—Stability of Connected Cruise Control

Jin I. Ge, Gábor Orosz, Dávid Hajdu, Tamás Insperger and Jeff Moehlis

Abstract The dynamics of connected vehicle systems are investigated where vehicles exchange information via wireless vehicle-to-vehicle (V2V) communication. In particular, connected cruise control (CCC) strategies are considered when using different delay configurations. Disturbance attenuation (string stability) along open chains is compared to the linear stability results using ring configuration. The results are summarized using stability diagrams that allow one to design the control gains for different delay values. Critical delay values are calculated and trade-offs between the different strategies are pointed out.

J.I. Ge (✉) · G. Orosz
Department of Mechanical Engineering, University of Michigan,
Ann Arbor, MI 48109, USA
e-mail: gejin@umich.edu

G. Orosz
e-mail: orosz@umich.edu

D. Hajdu
Department of Applied Mechanics, Budapest University of Technology and Economics,
Budapest 1111, Hungary
e-mail: hajdu@mm.bme.hu

T. Insperger
Department of Applied Mechanics, Budapest University of Technology and Economics
and MTA-BME Lendület Human Balancing Research Group, Budapest 1111, Hungary
e-mail: insperger@mm.bme.hu

J. Moehlis
Department of Mechanical Engineering, University of California, Santa Barbara,
CA 93106, USA
e-mail: moehlis@engineering.ucsb.edu

T. Insperger et al. (eds.), *Time Delay Systems*,
Advances in Delays and Dynamics 7, DOI 10.1007/978-3-319-53426-8_18

1 Introduction

Vehicular traffic has been fascinating researchers for decades and most of the early work has been focused on understanding how humans drive, in particular, how they control the longitudinal motion of vehicles [4, 7, 8]. In the last few decades, the so-called optimal velocity model [2, 10] gained popularity since this can reproduce a plethora of different large-scale traffic patterns observed empirically [20]. It also became evident that human drivers often trigger traffic jams due to their large reaction times and limited perception range [15].

In order to bypass this problem, the concept of adaptive cruise control (ACC) was created where the distance to the vehicle ahead is monitored by range sensors (e.g., radar, lidar) and the vehicle is actuated accordingly [11, 19]. By appropriate control design, one may guarantee attenuation of velocity perturbations between consecutive vehicles that is called string stability in the literature [18]. However, a relatively large penetration of ACC vehicles is required to change the behavior of the overall traffic flow [3], which may be difficult to reach due to the relatively high cost. Also, while the sensing delay of an ACC vehicle is significantly smaller than the human reaction time, it is still only able to monitor the motion of the vehicle immediately ahead.

Wireless vehicle-to-vehicle (V2V) communication can be used to obtain information from beyond the line of sight. Initial attempts focused on constructing platoons of ACC vehicles where the information broadcast by a designated platoon leader is utilized by the following vehicles. This strategy, called cooperative adaptive cruise control (CACC) [12, 21], can significantly improve the performance of the system but it requires all vehicles to be equipped with sensors and communication devices, and the number of vehicles involved is limited by the communication range. To eliminate such limitations the concept of connected cruise control (CCC) has been put forward that allows the inclusion of human-driven vehicles that may or may not broadcast information [1, 5, 13, 16, 22]. CCC utilizes all available information from multiple vehicles ahead and may be used to assist the human drivers, to complement sensor-based algorithms, or to automatically control the longitudinal motion of the vehicle. This increased flexibility makes CCC scalable for large connected vehicle systems.

However, intermittencies and packet drops lead to time delays in CCC. Such communication delays are typically larger than the sensing delays in ACC, though they are still smaller than human reaction time. Typically, one may expect that larger delays lead to degraded performance but time-delay systems may present counterintuitive behavior in terms of stability [9, 17]. In this paper, we investigate the simplest CCC scenario when each CCC vehicle utilizes information from the vehicle immediately ahead. While the received V2V information is delayed by the communication delay, information measured by on-board sensors may be available (almost) instantaneously. In this paper, we are asking the question whether one shall use these instantaneous values or shall delay them with the communication delay. We compare the different control strategies using stability charts where we identify gain combinations ensuring plant stability (stability in the lack of disturbances) and string

stability (attenuation of velocity disturbances arising ahead). We also identify trade-offs between the different strategies.

2 Modeling and Control Design with Delays

We consider connected cruise control strategies where each vehicle receives motion information from the vehicle immediately ahead via wireless V2V communication and uses this information to control its longitudinal motion. In particular, we consider control strategies of the form

$$\begin{aligned} \dot{s}(t) &= v(t)\,, \\ \dot{v}(t) &= F\big(s(t), v(t), s(t-\tau), v(t-\xi), s_{\mathrm{L}}(t-\sigma), v_{\mathrm{L}}(t-\sigma)\big)\,, \end{aligned} \tag{1}$$

where the dot stands for differentiation with respect to time t. Also, s, and s_{L} denote the position of the front bumpers of the vehicle and its immediate predecessor (called the leader), while v and v_{L} denote the corresponding velocities; see Fig. 1. The communication delay σ is caused by intermittencies and packet drops while the delays τ and ξ can be set when designing the controller. More precisely, we assume that the quantities s and v are available instantaneously through on-board sensors of high sampling rate but one may still use the delayed values in the control design as explained below. Indeed, τ and ξ may be set to zero or to be equal to σ.

In this paper, we base our control design on the optimal velocity model and consider three different delay scenarios, but all results can be generalized to car-following models of the general form (1); see [6, 15]. The first scenario is given by

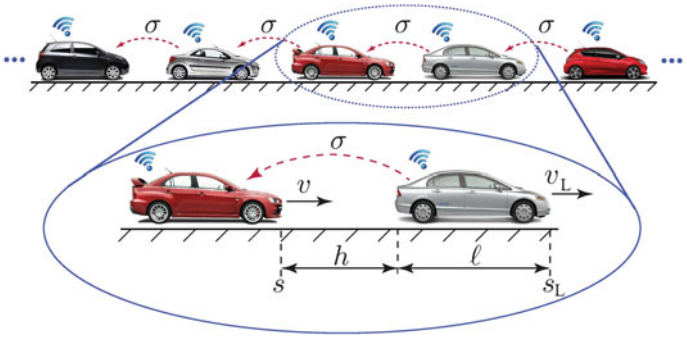

Fig. 1 Connected vehicles system where each vehicle receives information from the vehicle immediately ahead with the communication delay σ as indicated by the *red-dashed arrows*. The system can be constructed as the concatenation of leader–follower pairs shown below where the positions, the velocities, the headway, and the vehicle length are highlighted

$$\begin{aligned}\dot{s}(t) &= v(t)\,,\\ \dot{v}(t) &= \alpha\big(V(s_{\mathrm{L}}(t-\sigma)-s(t-\sigma)-\ell)-v(t-\sigma)\big)+\beta\big(W(v_{\mathrm{L}}(t-\sigma))-v(t-\sigma)\big)\,,\end{aligned} \tag{2}$$

which corresponds to matching all delays in the controller to the communication delay. Here, ℓ represents the length of the vehicle ahead (see Fig. 1) while the delayed value of the headway $h = s_{\mathrm{L}} - s - \ell$ appears in the monotonously increasing range policy function

$$V(h) = \begin{cases} 0 & \text{if} \quad h \le h_{\mathrm{st}}\,,\\ F(h) & \text{if} \quad h_{\mathrm{st}} < h < h_{\mathrm{go}}\,,\\ v_{\max} & \text{if} \quad h \ge h_{\mathrm{go}}\,. \end{cases} \tag{3}$$

That is, for small headways the vehicle intends to stop for safety reasons while for large headways it intends to travel with a chosen maximum speed. Between these we assume $F(h)$ to be strictly monotonously increasing such that $F(h_{\mathrm{st}}) = 0$ and $F(h_{\mathrm{go}}) = v_{\max}$. The simplest choice may be

$$F(h) = v_{\max}\frac{h-h_{\mathrm{st}}}{h_{\mathrm{go}}-h_{\mathrm{st}}}\,, \tag{4}$$

that is depicted in Fig. 2a where the time gap $T_{\mathrm{gap}} = (h_{\mathrm{go}} - h_{\mathrm{st}})/v_{\max}$ is highlighted. Notice that T_{gap} is constant for headway range $h_{\mathrm{st}} < h < h_{\mathrm{go}}$. However, the corresponding range policy is non-smooth at h_{st} and h_{go} which may lead to a "jerky ride". Thus, in this paper we use

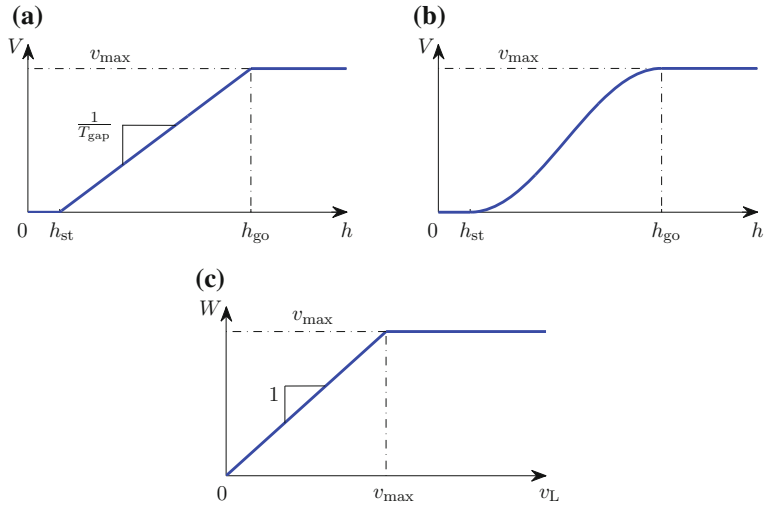

Fig. 2 **a**, **b** Range policies (3) with the middle sections given by (4) and (5). **c** Saturation function (6)

$$F(h) = \frac{v_{\max}}{2}\left(1 - \cos\left(\pi \frac{h - h_{\mathrm{st}}}{h_{\mathrm{go}} - h_{\mathrm{st}}}\right)\right), \tag{5}$$

that makes the range policy smooth as shown in Fig. 2b. Indeed, one may design range policies with higher level of smoothness as shown in [13].

The second term on the right-hand side of (2) contains the saturation function

$$W(v_{\mathrm{L}}) = \begin{cases} v_{\mathrm{L}} & \text{if} \quad v_{\mathrm{L}} \le v_{\max}\,, \\ v_{\max} & \text{if} \quad v_{\mathrm{L}} > v_{\max}\,, \end{cases} \tag{6}$$

shown in Fig. 2c, that is introduced to avoid the situation that the vehicle follows a leader whose velocity is larger than $v_{\max}$. Notice that when the leader's velocity is smaller than $v_{\max}$, the delayed value of the derivative of the headway $\dot{h} = v_{\mathrm{L}} - v$ appears on the right-hand side. Thus, in model (2) all quantities on the right hand side have clear physical meaning and we only compare quantities at the same time moment. When presenting the results below we use the numbers $h_{\mathrm{st}} = 5$ m, $h_{\mathrm{go}} = 35$ m, and $v_{\max} = 30$ m/s that corresponds to traffic data for human drivers [15].

Let us assume that the leader is traveling with a constant speed, that is, $s_{\mathrm{L}}(t) = v^* t + \bar{s}_{\mathrm{L}}$ and $v_{\mathrm{L}}(t) \equiv v^*$, where $0 < v^* < v_{\max}$ and $\bar{s}_{\mathrm{L}}$ is given by the initial condition. Then the follower admits the equilibrium

$$s(t) = v^* t + \bar{s}\,, \quad v(t) \equiv v^*\,, \quad \bar{s}_{\mathrm{L}} - \bar{s} - \ell = V^{-1}(v^*) = F^{-1}(v^*) := h^*\,. \tag{7}$$

In the vicinity of the equilibrium we define the time gap as $T_{\mathrm{gap}} = 1/V'(h^*) = 1/F'(h^*)$ which indeed changes with the equilibrium headway h^* (or equivalently with the equilibrium velocity v^*). Note that for $v^* = 0$ any constant headway smaller than h_{st} is possible while for $v^* = v_{\max}$ any constant headway larger than h_{go} may occur; see (3). For $v^* > v_{\max}$ no equilibrium exists and the headway between the leader and follower increases in time.

Since time delays often lead to instabilities and undesired oscillations in dynamic systems, one may try to eliminate some delays on the right hand side of (2). For example, the model

$$\begin{aligned} \dot{s}(t) &= v(t)\,, \\ \dot{v}(t) &= \alpha\big(V(s_{\mathrm{L}}(t-\sigma) - s(t-\sigma) - \ell) - v(t)\big) + \beta\big(W(v_{\mathrm{L}}(t-\sigma)) - v(t-\sigma)\big)\,, \end{aligned} \tag{8}$$

still contains the delayed values of the headway $h = s_{\mathrm{L}} - s - \ell$ and its derivative $\dot{h} = v_{\mathrm{L}} - v$ (when $v_{\mathrm{L}} \le v_{\max}$), but we consider the instantaneous value of the velocity v (as it may be measured by on-board sensors). The model (8) still satisfies the equilibrium (7) but in the first term on the right-hand side we compare a delayed value with an instantaneous value.

To further eliminate delays one may consider

$$\begin{aligned} \dot{s}(t) &= v(t)\,, \\ \dot{v}(t) &= \alpha\big(V(s_{\mathrm{L}}(t-\sigma) - s(t-\sigma) - \ell) - v(t)\big) + \beta\big(W(v_{\mathrm{L}}(t-\sigma)) - v(t)\big)\,, \end{aligned} \tag{9}$$

where both terms on the right-hand side compare delayed values to instantaneous values. In fact, the velocity difference in the second term can be created since the leader's velocity is received via wireless communication while the vehicle's own velocity is measured on board. This is not accessible when using range sensors to measure the headway and its derivative. The model (9) also satisfies the equilibrium (7).

One may argue that the delay in the position s may be neglected as well. However, in this case the desired equilibrium (7) cannot be achieved by the system. In particular, the equilibrium headway becomes $\bar{s}_{\mathrm{L}} - \bar{s} - \ell = V^{-1}(v^*) + v^*\sigma$ that may lead to safety hazards.

In the next section, we will compare the three models (2), (8) and (9) in terms of the stability and disturbance attenuation in the vicinity of the equilibrium (7) by plotting stability charts for different values of the communication delay σ.

3 Linear Stability Analysis

In order to analyze the behavior of the models proposed above, we consider two different configurations. In the *open chain configuration*, $N+1$ vehicles are placed on a straight road such that the motion of the head vehicle is prescribed. Then the system is viewed as an input–output system, such that the speed of the head vehicle v_{N+1} serves as the input and the speed of the tail vehicle v_1 serves as an output. In the *ring-road configuration*, N vehicles are placed on a circular road of length $L + N\ell$ (yielding $h^* = L/N$ and the periodic boundary conditions $s_{N+1} = s_1$, $v_{N+1} = v_1$).

When considering vehicles with identical range policies, there exists a uniform flow equilibrium where all vehicles travel with the same velocity while keeping the same headway; see (7). Our goal is to choose the gain parameters α and β such that the velocity perturbations are attenuated as they propagate backward along the vehicle chain, and the system is able to maintain the uniform flow equilibrium [13].

In order to analyze the dynamics in the vicinity of the equilibrium (7) one may define the perturbations $\tilde{s}_{\mathrm{L}}(t) = s_{\mathrm{L}}(t) - v^*t - \bar{s}_{\mathrm{L}}$, $\tilde{v}_{\mathrm{L}}(t) = v_{\mathrm{L}}(t) - v^*$, $\tilde{s}(t) = s(t) - v^*t - \bar{s}$, $\tilde{v}(t) = v(t) - v^*$ and linearize the above models about the equilibrium. In particular, model (2) results in

$$\begin{aligned} \dot{\tilde{s}}(t) &= \tilde{v}(t)\,, \\ \dot{\tilde{v}}(t) &= \alpha f^*\,(\tilde{s}_{\mathrm{L}}(t-\sigma) - \tilde{s}(t-\sigma)) + \beta\tilde{v}_{\mathrm{L}}(t-\sigma) - (\alpha+\beta)\tilde{v}(t-\sigma)\,, \end{aligned} \tag{10}$$

where we introduced the notation $f^* = V'(h^*) = F'(h^*)$. In this paper, we consider the equilibrium $v^* = 15$ m/s, that is, $h^* = 20$ m yielding the maximum $f^* = \pi/2$ 1/s; see (3, 5). This corresponds to the minimum value of the time gap $T_{\text{gap}} = 1/f^*$, which gives the worst case scenario in terms of stability.

Taking the Laplace transform with zero initial conditions one may derive the transfer function

$$\Gamma(s) = \frac{\tilde{V}(s)}{\tilde{V}_{\text{L}}(s)} = \frac{\beta s + \alpha f^*}{\mathrm{e}^{s\sigma} s^2 + (\alpha + \beta) s + \alpha f^*}, \tag{11}$$

where $\tilde{V}(s)$ and $\tilde{V}_{\text{L}}(s)$ denote the Laplace transform of $\tilde{v}(t)$ and $\tilde{v}_{\text{L}}(t)$, respectively. The transfer function allows us to evaluate stability and the amplitude ratio between the input and the output in steady state when applying sinusoidal input.

In order to ensure *plant stability* (that is, $\tilde{s}(t) \to 0$, $\tilde{v}(t) \to 0$ as $t \to 0$ when $\tilde{s}_{\text{L}}(t) \equiv 0$ and $\tilde{v}_{\text{L}}(t) \equiv 0$) one needs to make sure that the infinitely many poles of the transfer function (11) are located in the left half complex plane. In order to determine the stability boundary in the parameter plane of α and β, we consider two different types of stability loss. When a real pole crosses the imaginary axis, substituting $s = 0$ into the characteristic equation $\mathrm{e}^{s\sigma} s^2 + (\alpha + \beta) s + \alpha f^* = 0$ yields the stability boundary

$$\alpha = 0\,. \tag{12}$$

On the other hand, when a complex conjugate pair of poles crosses the imaginary axis, substituting $s = \mathrm{i}\Omega$ with $\Omega > 0$ into the characteristic equation and separating the real and imaginary parts result in the stability boundary

$$\begin{aligned} \alpha &= \frac{\Omega^2 \cos(\Omega\sigma)}{f^*}\,, \\ \beta &= \Omega \sin(\Omega\sigma) - \alpha\,, \end{aligned} \tag{13}$$

that is parameterized by the angular frequency Ω.

In the special case of $\sigma = 0$, (12) remains the same while (13) simplifies to $\beta = -\alpha$ as shown by the thick black lines in Fig. 3a. One may use the Routh–Hurwitz criteria to show that plant stability is achieved above the lines in the top right corner. For different values of $\sigma > 0$ the curves (12) and (13) are shown as thick black curves in the (β, α)-plane in Fig. 4a, c, e. One may apply Stépán's formulae [17] and show that stability is maintained inside the lobe-shaped domain. As the delay is increased, the plant stable domain shrinks and the size of the domain tends to zero as the delay is increased to infinity.

To ensure *string stability*, that is, attenuation of velocity perturbations between the leader and the follower, we consider sinusoidal excitation $\tilde{v}_{\text{L}}(t) = v_{\text{L}}^{\text{amp}} \sin(\omega t)$, which (assuming plant stability) leads to the steady state response $\tilde{v}^{\text{ss}}(t) = v^{\text{amp}} \sin(\omega t + \psi)$, where $v^{\text{amp}}/v_{\text{L}}^{\text{amp}} = |\Gamma(\mathrm{i}\omega)|$ and $\psi = \angle\Gamma(\mathrm{i}\omega)$. Requiring $|\Gamma(\mathrm{i}\omega)| < 1$ for all $\omega > 0$ ensures attenuation of sinusoidal signals and, as superposition holds for

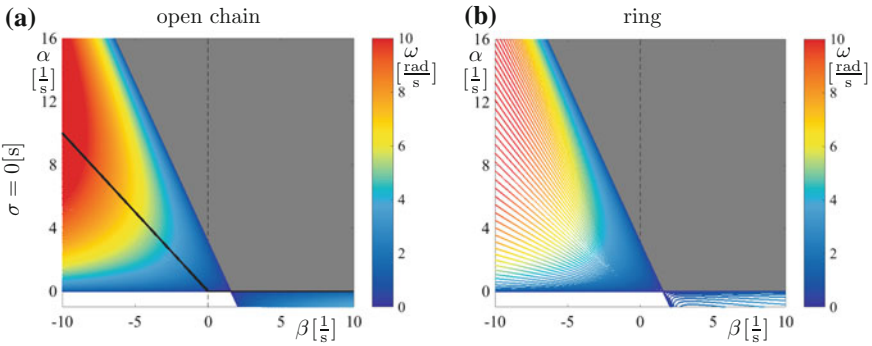

Fig. 3 Stability diagrams for the system (10) for $\sigma = 0$ using the open chain configuration (*left*) and the ring configuration (*right*). The system is plant stable above the thick *black lines*. The *gray-shaded* region indicates string stability while coloring refers to the oscillation frequencies as indicated by the *color bar*

linear systems, for the linear combination of those signals. This condition may be rewritten as $\omega^2 P(\omega) > 0$ where

$$P(\omega) = \omega^2 + 2\alpha\beta + \alpha^2 - 2(\alpha + \beta)\omega \sin(\omega\sigma) - 2\alpha f^* \cos(\omega\sigma)\,. \tag{14}$$

The stability boundaries can be identified corresponding to the minima of P becoming negative at $\omega_{\mathrm{cr}} > 0$ that is defined by

$$\begin{aligned} P(\omega_{\mathrm{cr}}) &= 0\,, \\ \frac{\partial P}{\partial \omega}(\omega_{\mathrm{cr}}) &= 0\,, \end{aligned} \tag{15}$$

while satisfying $\frac{\partial^2 P}{\partial \omega^2}(\omega_{\mathrm{cr}}) > 0$. Solving this for α and β one may obtain the string stability boundaries parameterized by ω_{cr} as

$$\begin{aligned} \alpha &= a \pm \sqrt{a^2 + b}\,, \\ \beta &= \frac{\omega_{\mathrm{cr}} + \alpha f^* \sigma \sin(\omega_{\mathrm{cr}}\sigma)}{\sin(\omega_{\mathrm{cr}}\sigma) + \omega_{\mathrm{cr}}\sigma \cos(\omega_{\mathrm{cr}}\sigma)} - \alpha\,, \end{aligned} \tag{16}$$

where

$$\begin{aligned} a &= \frac{\omega_{\mathrm{cr}}(f^*\sigma - 1) + f^* \sin(\omega_{\mathrm{cr}}\sigma)\cos(\omega_{\mathrm{cr}}\sigma)}{(2f^*\sigma - 1)\sin(\omega_{\mathrm{cr}}\sigma) - \omega_{\mathrm{cr}}\sigma\cos(\omega_{\mathrm{cr}}\sigma)}\,, \\ b &= \frac{\omega_{\mathrm{cr}}^2\big(\sin(\omega_{\mathrm{cr}}\sigma) - \omega_{\mathrm{cr}}\sigma\cos(\omega_{\mathrm{cr}}\sigma)\big)}{(2f^*\sigma - 1)\sin(\omega_{\mathrm{cr}}\sigma) - \omega_{\mathrm{cr}}\sigma\cos(\omega_{\mathrm{cr}}\sigma)}\,. \end{aligned} \tag{17}$$

For $\omega_{\rm cr} = 0$, the equalities $|\Gamma(0)| = 1$ and $\frac{\partial|\Gamma|}{\partial\omega}(0) = 0$ always hold. Thus for string stability we need $\frac{\partial^2|\Gamma|}{\partial\omega^2}(0) < 0$ which is equivalent to $P(0) = \alpha(\alpha + 2\beta - 2f^*) > 0$. That is, one of the boundaries is equivalent to the plant stability boundary (12) while the other is given by

$$\alpha = 2(f^* - \beta)\,. \tag{18}$$

Notice that this zero-frequency boundary does not depend on the delay σ.

In the special case of $\sigma = 0$, only the string stability boundaries (12) and (18) appear as shown by the straight lines bounding the gray string stable domain in Fig. 3a. The coloring outside the string stable area corresponds to the solution of $P(\omega) = \omega^2 + \alpha(\alpha + 2\beta - 2f^*) = 0$ for the frequency ω. The coloring indicates that string stability is lost for low frequencies. For different values of $\sigma > 0$ the stability boundaries (12, 16–18) enclose the gray-shaded string stability domain in the (β, α)-plane as depicted in Fig. 4a, c, e. The coloring outside the string stable area corresponds to the solution of $P(\omega) = 0$ for the frequency ω (cf. (14)). When there exist multiple solutions we use the largest ω value. The coloring indicates that when leaving the string stable area toward the left, string stability is still lost at low frequencies. On the other hand, leaving the area to the right, high-frequency string instability occurs. To demonstrate this behavior we marked the points A, B, C on Fig. 4a and plot the corresponding amplification ratios as a function of the frequencies in Fig. 5a. Indeed, for case B the amplification ratio stays below 1 for all frequencies. For cases A and C it exceeds 1 for low and high frequencies, respectively.

One may observe that as the delay σ increases the string stable domain shrinks and for $\sigma = 0.3$ s it almost disappears. In fact, there exists a critical value of the delay such that for $\sigma > \sigma_{\rm cr}$ there exist no gain combinations that can ensure string stability. To calculate the critical delay one may use the L'Hospital rule to show that for $\omega_{\rm cr} \to 0$ formulae (16, 17) yield the points

$$\begin{aligned}(\alpha^+,\, \beta^+) &= \left(\frac{2f^*\sigma - 1}{\sigma(f^*\sigma - 1)},\, \frac{2(f^*\sigma)^2 - 4f^*\sigma + 1}{2\sigma(f^*\sigma - 1)}\right),\\ (\alpha^-,\, \beta^-) &= \left(0,\, \frac{1}{2\sigma}\right),\end{aligned} \tag{19}$$

which are located along the stability boundary around the yellow shading in Fig. 4a. These points move closer to each other when the delay increases and coincide when the delay takes the value

$$\sigma_{\rm cr} = \frac{1}{2f^*} = \frac{T_{\rm gap}}{2}\,. \tag{20}$$

Finally notice that for an open chain of $N + 1$ vehicles, one may derive the head-to-tail transfer function $(\Gamma(s))^N = \tilde{V}_1(s)/\tilde{V}_{N+1}(s)$ between the head vehicle $N + 1$ and

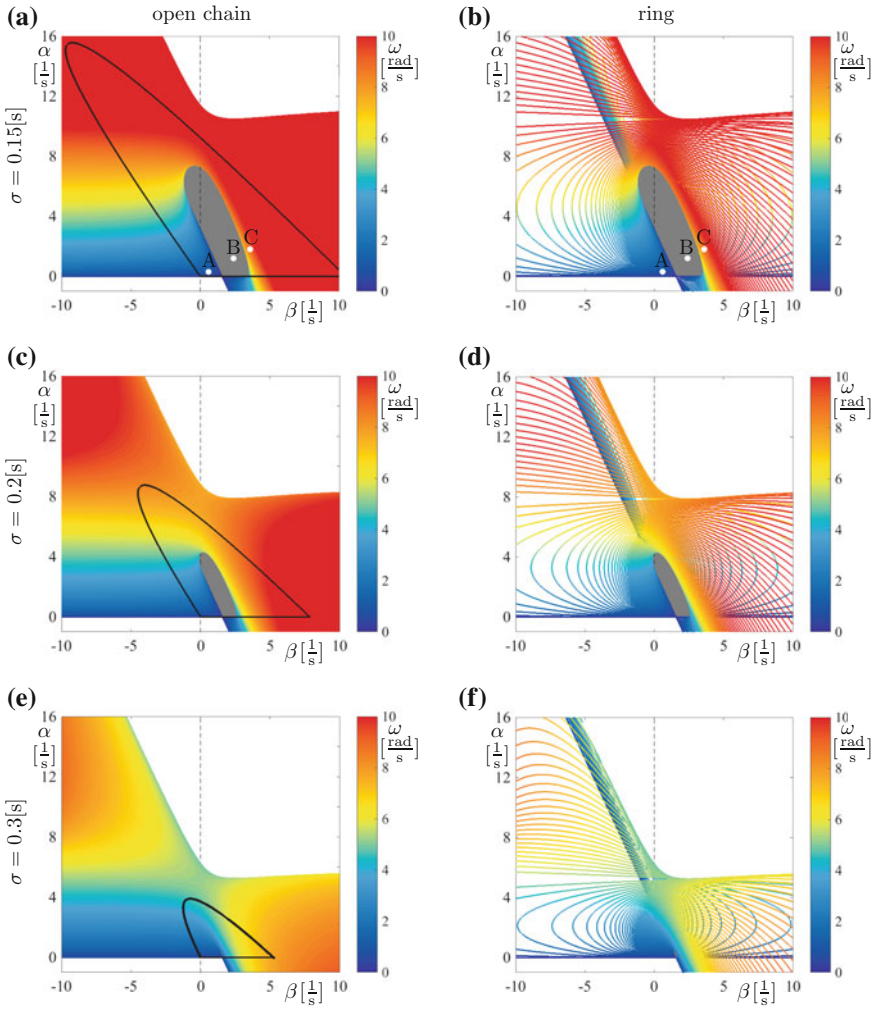

Fig. 4 Stability diagrams for the system (10) for different delay values as indicated using the open chain configuration (*left*) and the ring configuration (*right*). The system is plant stable within the lobe-shaped domain enclosed by the thick *black curve*. The *gray-shaded* region indicates string stability while coloring refers to the oscillation frequencies as indicated by the *color bar*

the tail vehicle 1. Thus, the string stability condition still remains the same independent of N.

When having N vehicles on a ring-road, one may define the state $X = [\tilde{s}_1, \tilde{v}_1, \ldots, \tilde{s}_N, \tilde{v}_N]^T$ where T denotes the transpose. Then (10) can be written into the compact form

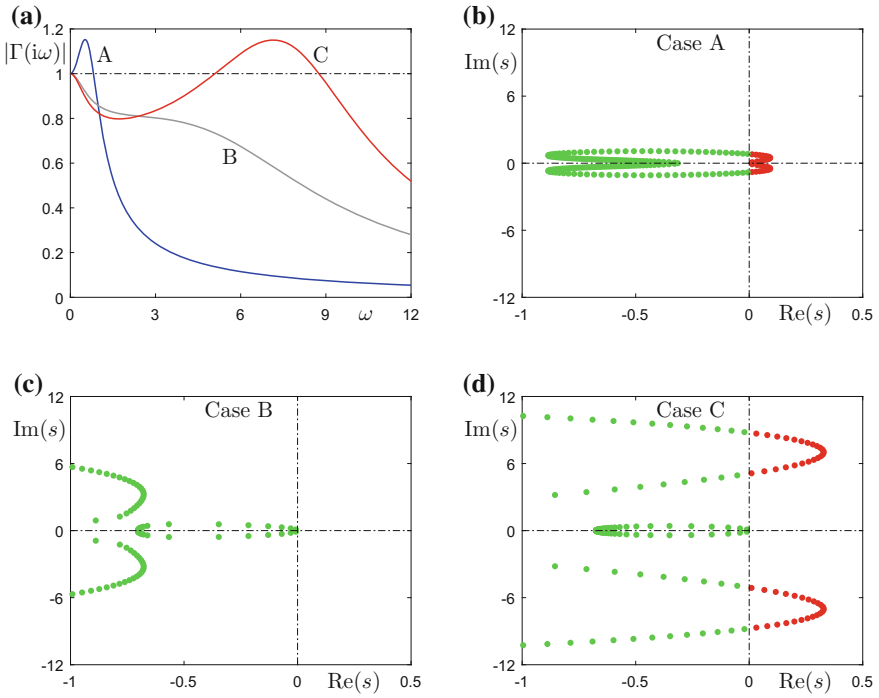

Fig. 5 **a** Amplification ratios for the points marked A, B, C in Fig. 4a, b when considering two consecutive cars in an open chain. **b**, **c**, **d** Corresponding characteristic roots in case of the ring configuration

$$\begin{aligned}\dot{X}(t) &= (\mathbf{I}\otimes\mathbf{a})X(t) + (\mathbf{I}\otimes\mathbf{b} + \mathbf{R}\otimes\mathbf{c})X(t-\sigma)\\ &= \begin{bmatrix}\mathbf{a} & & \\ & \ddots & \\ & & \mathbf{a}\end{bmatrix}X(t) + \begin{bmatrix}\mathbf{b} & \mathbf{c} & \\ & \ddots & \ddots \\ & & \mathbf{b} \\ \mathbf{c} & & \mathbf{b}\end{bmatrix}X(t-\sigma)\,,\end{aligned} \tag{21}$$

where $\otimes$ denotes the Kronecker product and $\mathbf{I}$ is the N-dimensional identity matrix. Also, the N-dimensional matrix $\mathbf{R}$ is given by

$$\mathbf{R} = \begin{bmatrix}0 & 1 & 0 & \cdots & 0\\ 0 & 0 & 1 & \ddots & \vdots\\ \vdots & & \ddots & \ddots & 0\\ 0 & 0 & \cdots & 0 & 1\\ 1 & 0 & \cdots & 0 & 0\end{bmatrix}, \tag{22}$$

while the two-dimensional nonzero blocks are

$$\mathbf{a} = \begin{bmatrix} 0 & 1 \\ 0 & 0 \end{bmatrix}, \quad \mathbf{b} = \begin{bmatrix} 0 & 0 \\ -\alpha f^* & -(\alpha+\beta) \end{bmatrix}, \quad \mathbf{c} = \begin{bmatrix} 0 & 0 \\ \alpha f^* & \beta \end{bmatrix}. \tag{23}$$

Then one can block-diagonalize the matrices in (21) using the coordinate transformation

$$X = (\mathbf{T} \otimes \mathbf{I})Z, \tag{24}$$

where the N-dimensional matrix $\mathbf{T}$ is constructed from the eigenvectors of $\mathbf{R}$ while $\mathbf{I}$ is the two-dimensional identity matrix. This yields

$$\dot{Z}(t) = \begin{bmatrix} \mathbf{a} & & \\ & \ddots & \\ & & \mathbf{a} \end{bmatrix} Z(t) + \begin{bmatrix} \mathbf{b}+\mathbf{c} & & & \\ & \mathbf{b}+\mathrm{e}^{\mathrm{i}\frac{2\pi}{N}}\mathbf{c} & & \\ & & \ddots & \\ & & & \mathbf{b}+\mathrm{e}^{\mathrm{i}\frac{2(N-1)\pi}{N}}\mathbf{c} \end{bmatrix} Z(t-\sigma), \tag{25}$$

where $\mathrm{e}^{\mathrm{i}\frac{2k\pi}{N}}$, for $k = 0, 1, \ldots, N-1$ are the eigenvalues of the matrix $\mathbf{R}$ in (22). The corresponding eigenvectors, that constitute the columns of $\mathbf{T}$ in (24), are given by $[1, \mathrm{e}^{\mathrm{i}\frac{2k\pi}{N}}, \mathrm{e}^{\mathrm{i}\frac{2k\pi}{N}2}, \ldots, \mathrm{e}^{\mathrm{i}\frac{2k\pi}{N}(N-1)}]^{\mathrm{T}}$, for $k = 0, 1, \ldots, N-1$. Thus, the physical meaning of k is a discrete wave number of the appearing traveling waves and the corresponding spatial wavelengths are $\Lambda = (L + N\ell)/k$ for $k \leq N/2$ and $\Lambda = (L + N\ell)/(N-k)$ for $k > N/2$. In other words, the same spatial pattern arises for wave numbers k and $N-k$.

The block-diagonal matrices in (25) allow us to analyze the stability of the traveling waves separately for each wave number k. In particular, using the trial solution $Z(t) \sim \mathrm{e}^{st}$ one may obtain the characteristic equation

$$\prod_{k=0}^{N-1} \det\left[s\mathbf{I} - \mathbf{a} - \left(\mathbf{b} + \mathrm{e}^{\mathrm{i}\frac{2k\pi}{N}}\mathbf{c}\right)\mathrm{e}^{-s\sigma}\right] = 0. \tag{26}$$

Using the definitions (23), this yields

$$\mathrm{e}^{s\sigma}s^2 + (\alpha+\beta)s + \alpha f^* - \left(\beta s + \alpha f^*\right)\mathrm{e}^{\mathrm{i}\frac{2k\pi}{N}} = 0 \tag{27}$$

for $k = 0, 1, \ldots, N-1$. Notice that using the transfer function (11) and the periodic boundary conditions imply $(\Gamma(s))^N = 1$ and taking the N-th root results in the characteristic equation (27).

The system is stable if the characteristic roots are located in the left half complex plane for all k. To determine the corresponding stability boundaries we consider the critical scenarios when characteristic roots cross the imaginary axis. For wavenumber $k = 0$, one may notice $s = 0$ satisfies (27) for all values of α and β. This corresponds to the translational symmetry of the ring configuration: the system is invariant when shifting all vehicles with the same distance along the road [14]. For wavenumbers $k > 0$, substituting $s = 0$ into (27) yields the stability boundary (12).

On the other hand, when considering that a pair of complex conjugate roots crosses the imaginary axis, substituting $s = \pm \mathrm{i}\omega$ into (27) results in the stability boundaries

$$\begin{aligned} \alpha &= \frac{\omega^2\big(\cos(\omega\sigma) - \cos(\omega\sigma - \frac{2k\pi}{N})\big)}{-\omega\sin(\frac{2k\pi}{N}) + 2f^*\big(1 - \cos(\frac{2k\pi}{N})\big)}\,, \\ \beta &= \frac{-\omega^2\cos(\omega\sigma) + f^*\omega\big(\sin(\omega\sigma) - \sin(\omega\sigma - \frac{2k\pi}{N})\big)}{-\omega\sin(\frac{2k\pi}{N}) + 2f^*\big(1 - \cos(\frac{2k\pi}{N})\big)} \end{aligned} \tag{28}$$

for $k = 0, 1, \ldots, N-1$ as depicted in Fig. 3b and in Fig. 4b, d, f for different values of the delay σ while considering $N = 100$ vehicles. Each curve is parameterized by the frequency ω as highlighted by the color code. Notice the remarkable similarity between the stability charts shown in the left and the right of Fig. 4 despite the fact that panels (a, c, e) correspond to the steady state response of the open chain while panels (b, d, f) correspond to the transient response of the ring configuration. To further emphasize this similarity we plot the characteristic roots (the solutions of (27)) in the complex plane in Fig. 5b, c, d for the points marked A, B, C in Fig. 4b. For cases A and C the crossing frequencies in Fig. 5a and in Fig. 5b, d show a good correspondence.

Linearizing the model (8) about the equilibrium (7) yields

$$\begin{aligned} \dot{\tilde{s}}(t) &= \tilde{v}(t)\,, \\ \dot{\tilde{v}}(t) &= \alpha f^*\left(\tilde{s}_{\mathrm{L}}(t-\sigma) - \tilde{s}(t-\sigma)\right) + \beta\tilde{v}_{\mathrm{L}}(t-\sigma) - \alpha\tilde{v}(t) - \beta\tilde{v}(t-\sigma)\,. \end{aligned} \tag{29}$$

Taking the Laplace transform with zero initial conditions we obtain the transfer function

$$\Gamma(s) = \frac{\tilde{V}(s)}{\tilde{V}_{\mathrm{L}}(s)} = \frac{\beta s + \alpha f^*}{\mathrm{e}^{s\sigma}(s^2 + \alpha s) + \beta s + \alpha f^*}\,. \tag{30}$$

The corresponding plant stability boundaries are given by (12) and

$$\begin{aligned} \alpha &= \frac{\Omega^2\cos(\Omega\sigma)}{f^* - \Omega\sin(\Omega\sigma)}\,, \\ \beta &= \Omega\sin(\Omega\sigma) - \alpha\cos(\Omega\sigma)\,, \end{aligned} \tag{31}$$

that are shown as thick black curves in the (β, α)-plane in Fig. 6a, c, e. Applying Stépán's formulae [17] shows that the system is plant stable when parameters are chosen from the region above the black curves. Again, increasing the delay leads to smaller plant stable domains.

In this case, the string stability condition can be rewritten as $\omega Q(\omega) > 0$ where

$$Q(\omega) = \omega^3 + \alpha^2\omega - 2(\alpha^2 f^* + \beta\omega^2)\sin(\omega\sigma) + 2(\alpha\beta - \alpha f^*)\omega\cos(\omega\sigma)\,. \tag{32}$$

For $\omega_{\rm cr} > 0$ the string stability boundaries can be obtained by substituting P with Q in (15) which yields

$$\begin{aligned} &\sum_{p=0}^{3} a_p \alpha^p = 0\,, \\ &\beta = \frac{\omega_{\rm cr}^3 + \alpha^2\omega_{\rm cr} - 2\alpha f^*\big(\alpha\sin(\omega_{\rm cr}\sigma) + \omega_{\rm cr}\cos(\omega_{\rm cr}\sigma)\big)}{2\omega_{\rm cr}\big(\omega_{\rm cr}\sin(\omega_{\rm cr}\sigma) - \alpha\cos(\omega_{\rm cr}\sigma)\big)}\,, \end{aligned} \tag{33}$$

where

$$\begin{aligned} a_0 &= \omega_{\rm cr}^4\cos(\omega_{\rm cr}\sigma)\big(-\sin(\omega_{\rm cr}\sigma) + \omega_{\rm cr}\sigma\cos(\omega_{\rm cr}\sigma)\big)\,, \\ a_1 &= \omega_{\rm cr}^2\cos(\omega_{\rm cr}\sigma)\big(\omega_{\rm cr}^2\sigma\sin(\omega_{\rm cr}\sigma) - 2f^*\sin(\omega_{\rm cr}\sigma)\cos(\omega_{\rm cr}\sigma) + 2\omega_{\rm cr}\cos(\omega_{\rm cr}\sigma) - 2f^*\omega_{\rm cr}\sigma\big)\,, \\ a_2 &= \omega_{\rm cr}\cos(\omega_{\rm cr}\sigma)\big(\omega_{\rm cr}\sin(\omega_{\rm cr}\sigma) - 4f^*\sin^2(\omega_{\rm cr}\sigma) + \omega_{\rm cr}^2\sigma\cos(\omega_{\rm cr}\sigma)\big)\,, \\ a_3 &= \cos(\omega_{\rm cr}\sigma)\big(\omega_{\rm cr}^2\sigma\sin(\omega_{\rm cr}\sigma) + 2f^*\sin(\omega_{\rm cr}\sigma)\cos(\omega_{\rm cr}\sigma) - 2f^*\omega_{\rm cr}\sigma\big)\,. \end{aligned} \tag{34}$$

For $\omega_{\rm cr} = 0$, the inequality $\frac{\partial^2|\Gamma|}{\partial\omega^2}(0) < 0$ is equivalent to $\frac{\partial Q}{\partial\omega}(0) = \alpha\big((1-2f^*\sigma)\alpha + 2\beta - 2f^*\big) > 0$, that yields the boundaries (12) and

$$\alpha = \frac{2(f^* - \beta)}{1 - 2f^*\sigma}\,. \tag{35}$$

That is, in this case, the gradient of the zero-frequency boundary is influenced by the delay as shown by the boundary on the left of the gray string stable region in Figs. 3a and 6a, c, e. Here the coloring corresponds to the solution of $Q(\omega) = 0$ for the frequency ω (cf.(32)). Again, on the left string stability is lost at low frequencies while on the right high-frequency string instability occurs. The string stable domain is not closed from above but it still shrinks as the delay increases and it disappears when the delay exceeds

$$\sigma_{\rm cr} \approx \frac{0.785}{f^*} = 0.785\,T_{\rm gap}\,, \tag{36}$$

but this value cannot be calculated analytically.

When comparing Figs. 4a, c, e and 6a, c, e one may notice a trade-off. While the critical delay is significantly larger in the latter case, it also requires larger gains to make the systems string stable as the delay is increased. This may be difficult to achieve in practice due to the saturation of the actuators.

In case of the ring configuration we may still write the system into the form (21) where $\mathbf{R}$ is still given by (22), but the blocks are given by

$$\mathbf{a} = \begin{bmatrix} 0 & 1 \\ 0 & -\alpha \end{bmatrix}\,, \quad \mathbf{b} = \begin{bmatrix} 0 & 0 \\ -\alpha f^* & -\beta \end{bmatrix}\,, \quad \mathbf{c} = \begin{bmatrix} 0 & 0 \\ \alpha f^* & \beta \end{bmatrix}\,. \tag{37}$$

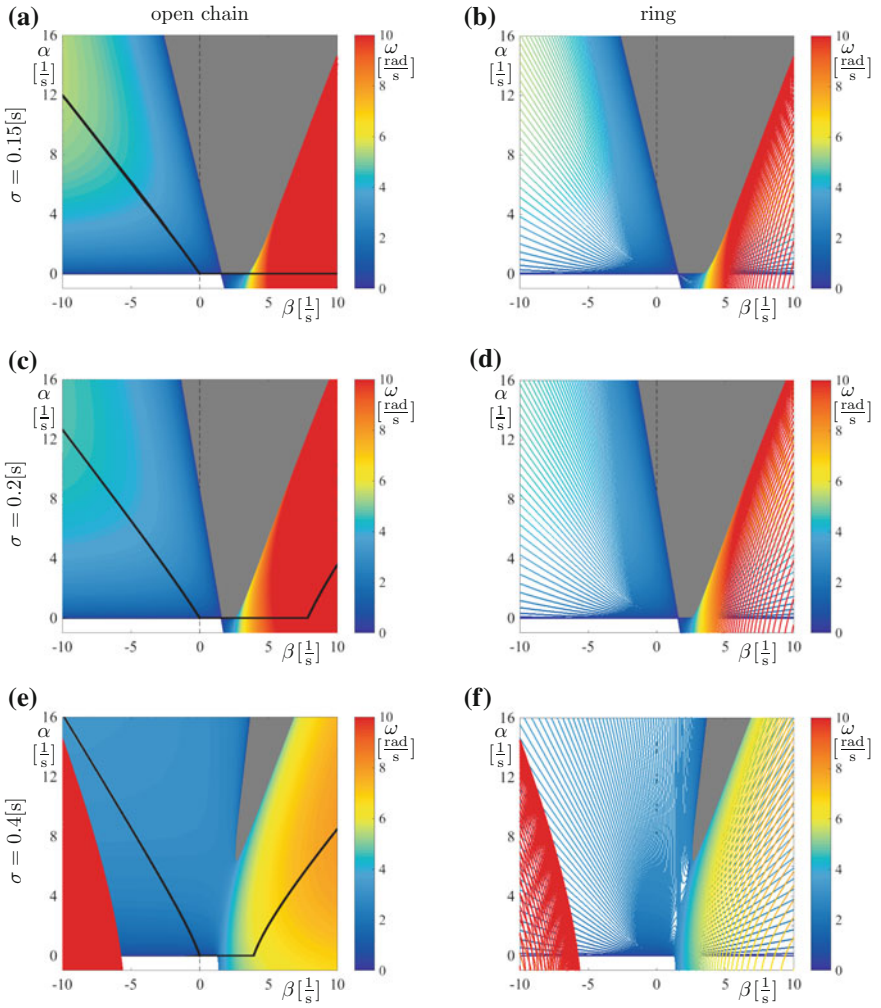

Fig. 6 Stability diagrams for the system (29) using the open chain configuration (*left*) and the ring configuration (*right*). The same notation is used as in Fig. 4

After obtaining the block-diagonal form (25) we can obtain the characteristic equation in the form (26) that yields

$$e^{s\sigma}\left(s^2 + \alpha s\right) + \beta s + \alpha f^* - \left(\beta s + \alpha f^*\right)e^{i\frac{2k\pi}{N}} = 0 \tag{38}$$

for $k = 0, 1, \ldots, N-1$. The corresponding stability boundaries are given by

$$\begin{aligned} \alpha &= \frac{\omega^2\big(\cos(\omega\sigma) - \cos(\omega\sigma - \frac{2k\pi}{N})\big)}{-\omega\big(\sin(\omega\sigma) - \sin(\omega\sigma - \frac{2k\pi}{N})\big) + 2f^*\big(1 - \cos(\frac{2k\pi}{N})\big)}\,, \\ \beta &= \frac{-\omega^2 + f^*\omega\big(\sin(\omega\sigma) - \sin(\omega\sigma - \frac{2k\pi}{N})\big)}{-\omega\big(\sin(\omega\sigma) - \sin(\omega\sigma - \frac{2k\pi}{N})\big) + 2f^*\big(1 - \cos(\frac{2k\pi}{N})\big)} \end{aligned} \tag{39}$$

for $k = 0, 1, \ldots, N-1$ as depicted in Fig. 6b, d, f for different values of the delay σ while considering $N = 100$ vehicles. Again, comparing panels (a, c, e) to panels (b, d, f) shows very good correspondence with each other.

Finally, the linearization of (9) about the equilibrium (7) takes the form

$$\begin{aligned} \dot{\tilde{s}}(t) &= \tilde{v}(t)\,, \\ \dot{\tilde{v}}(t) &= \alpha f^*\left(\tilde{s}_{\mathrm{L}}(t-\sigma) - \tilde{s}(t-\sigma)\right) + \beta\tilde{v}_{\mathrm{L}}(t-\sigma) - (\alpha+\beta)\tilde{v}(t)\,, \end{aligned} \tag{40}$$

and the corresponding transfer function is given by

$$\Gamma(s) = \frac{\tilde{V}(s)}{\tilde{V}_{\mathrm{L}}(s)} = \frac{\beta s + \alpha f^*}{\mathrm{e}^{s\sigma}\left(s^2 + (\alpha+\beta)s\right) + \alpha f^*}\,. \tag{41}$$

Then the plant stability boundaries are given by (12) and

$$\begin{aligned} \alpha &= \frac{\Omega^2}{f^*\cos(\Omega\sigma)}\,, \\ \beta &= \Omega\tan(\Omega\sigma) - \alpha\,, \end{aligned} \tag{42}$$

that are displayed as thick black curves in Fig. 7a, c, e. According to Stépán's formulae [17] the system is plant stable above the curves and increasing the delay still deteriorates plant stability (though this effect is not so pronounced when comparing to the other two cases discussed above).

Again the string stability condition can be written as $\omega R(\omega) > 0$ where

$$R(\omega) = \omega^3 + \alpha^2\omega + 2\alpha\beta\omega - 2\alpha f^*(\alpha+\beta)\sin(\omega\sigma) - 2\alpha f^*\omega\cos(\omega\sigma)\,, \tag{43}$$

and substituting P with R in (15) results in the string stability boundaries

$$\begin{aligned} \alpha &= \hat{a} \pm \sqrt{\hat{a}^2 + \hat{b}}\,, \\ \beta &= \frac{\omega_{\mathrm{cr}}^3 + \alpha^2\omega_{\mathrm{cr}} - 2\alpha f^*\left(\alpha\sin(\omega_{\mathrm{cr}}\sigma) + \omega_{\mathrm{cr}}\cos(\omega_{\mathrm{cr}}\sigma)\right)}{2\alpha\left(f^*\sin(\omega_{\mathrm{cr}}\sigma) - \omega_{\mathrm{cr}}\right)}\,, \end{aligned} \tag{44}$$

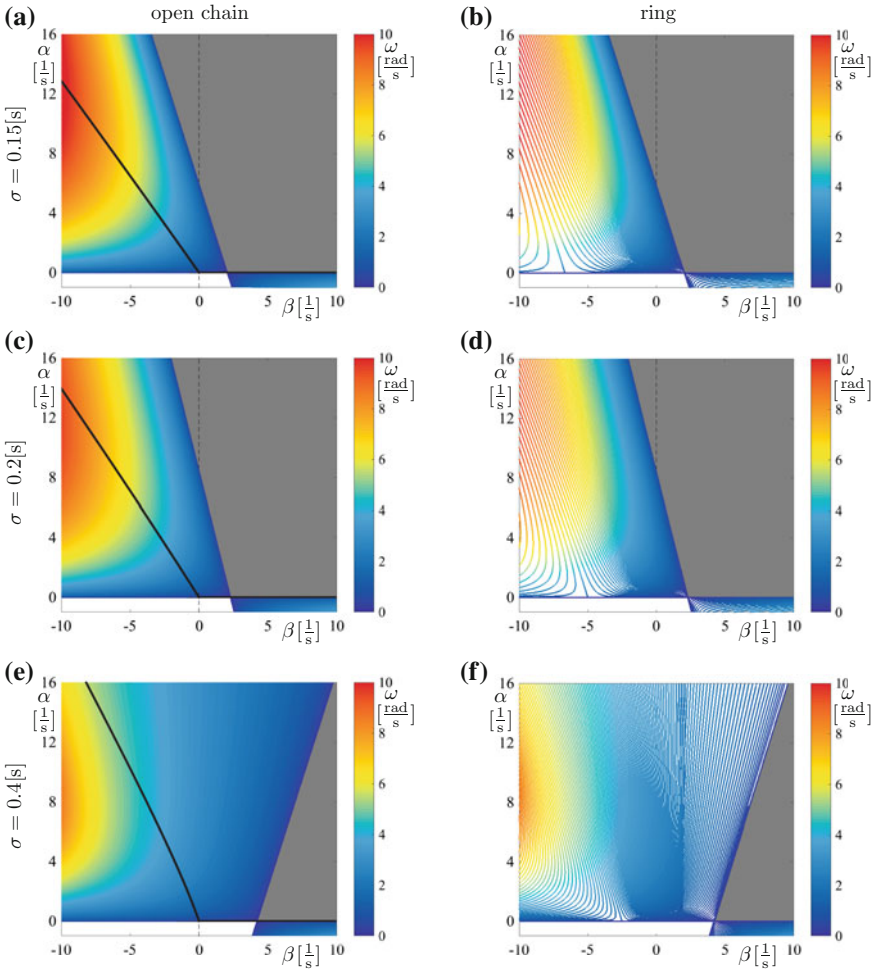

Fig. 7 Stability diagrams for the system (40) using the open chain configuration (*left*) and the ring configuration (*right*). The same notation is used as in Fig. 4

where

$$\begin{aligned}\hat{a} &= \frac{-\omega_{\text{cr}}^2\sigma\sin(\omega_{\text{cr}}\sigma) - f^*\sin(\omega_{\text{cr}}\sigma)\cos(\omega_{\text{cr}}\sigma) + f^*\omega_{\text{cr}}\sigma}{\sin(\omega_{\text{cr}}\sigma) - \omega_{\text{cr}}\sigma\cos(\omega_{\text{cr}}\sigma)}\,,\\ \hat{b} &= \frac{\omega_{\text{cr}}^2\left(3f^*\sin(\omega_{\text{cr}}\sigma) - f^*\omega_{\text{cr}}\sigma\cos(\omega_{\text{cr}}\sigma) - 2\omega_{\text{cr}}\right)}{f^*\left(\sin(\omega_{\text{cr}}\sigma) - \omega_{\text{cr}}\sigma\cos(\omega_{\text{cr}}\sigma)\right)}\,.\end{aligned} \tag{45}$$

However, we remark that these do not give stability boundaries in the physically realistic parameter ranges.

For $\omega_{\rm cr} = 0$, we obtain $\frac{\partial R}{\partial \omega}(0) = \alpha\big((1-2f^*\sigma)\alpha + 2(1-f^*\sigma)\beta - 2f^*\big) > 0$, that yields the boundaries (12) and

$$\alpha = \frac{2\big(f^* - (1-f^*\sigma)\beta\big)}{1-2f^*\sigma}\,. \tag{46}$$

That is, both the gradient and the position of the zero-frequency boundary is influenced by the delay which can be observed when looking at the left boundary in Figs. 3a and 6a, c, e. As shown by the coloring, only low-frequency string instability occurs and the gray string stable domain is open from above and from the right. By investigating when the gradient of (46) becomes zero one can calculate the critical delay

$$\sigma_{\rm cr} = \frac{1}{f^*} = T_{\rm gap}\,, \tag{47}$$

above which the string stable domain disappears.

Again comparing Figs. 4a, c, e, 6a, c, e, and 7a, c, e one may notice that the critical delay increases but larger gains are required to make the system string stable which may not be possible due to the limitation of the actuators.

In case of the ring configuration (25) contains

$$\mathbf{a} = \begin{bmatrix} 0 & 1 \\ 0 & -(\alpha+\beta) \end{bmatrix}, \quad \mathbf{b} = \begin{bmatrix} 0 & 0 \\ -\alpha f^* & 0 \end{bmatrix}, \quad \mathbf{c} = \begin{bmatrix} 0 & 0 \\ \alpha f^* & \beta \end{bmatrix}, \tag{48}$$

while (26) yields

$$\mathrm{e}^{s\sigma}\big(s^2 + (\alpha+\beta)s\big) + \beta s + \alpha f^* - \alpha f^* \mathrm{e}^{\mathrm{i}\frac{2k\pi}{N}} = 0\,, \tag{49}$$

resulting in the stability boundaries

$$\begin{aligned} \alpha &= \frac{\omega^2\big(1-\cos(\omega\sigma - \frac{2k\pi}{N})\big)}{\omega\sin(\omega\sigma - \frac{2k\pi}{N}) + f^*\big(1-\cos(\frac{2k\pi}{N}) + \cos(\omega\sigma) - \cos(\omega\sigma - \frac{2k\pi}{N})\big)}\,, \\ \beta &= \frac{-\omega^2 + f^*\omega\big(\sin(\omega\sigma) - \sin(\omega\sigma - \frac{2k\pi}{N})\big)}{\omega\sin(\omega\sigma - \frac{2k\pi}{N}) + f^*\big(1-\cos(\frac{2k\pi}{N}) + \cos(\omega\sigma) - \cos(\omega\sigma - \frac{2k\pi}{N})\big)} \end{aligned} \tag{50}$$

for $k = 0, 1, \ldots, N-1$ as shown in Fig. 7b, d, f for different σ values and $N = 100$ vehicles. Indeed, panels (a, c, e) show very good correspondence with panels (b, d, f).

4 Conclusion

The effect of time delays has been investigated in connected cruise control scenarios where each vehicle controls its longitudinal motion based on the V2V information received from the vehicles immediately ahead. In order to evaluate the stability of uniform traffic flow we considered open chain and ring configurations and our results show that these configurations give the same results when the number of vehicles is large enough. We also demonstrated that as the delay increases the stable areas shrink, and that when the delay exceeds a critical value no gain combinations can stabilize the uniform flow. Moreover, using the instantaneous values of quantities measured on board may not necessarily improve the performance. On one hand, one may increase the critical value of the delay, but on the other hand it requires larger gains to stabilize the system (that may not be available due to actuator limitations). Thus, it may in fact be beneficial to delay the values of the on-board quantities to achieve high-performance CCC design.

References

1. Avedisov, S.S., Orosz, G.: Nonlinear network modes in cyclic systems with applications to connected vehicles. J. Nonlinear Sci. **25**, 1015–1049 (2015)
2. Bando, M., Hasebe, K., Nakanishi, K., Nakayama, A.: Analysis of optimal velocity model with explicit delay. Phys. Rev. E **58**(5), 5429–5435 (1998)
3. Davis, L.C.: Effect of adaptive cruise control systems on traffic flow. Phys. Rev. E **69**(6), 066–110 (2004)
4. Gazis, D.C., Herman, R., Rothery, R.W.: Nonlinear follow-the-leader models of traffic flow. Oper. Res. **9**(4), 545–567 (1961)
5. Ge, J.I., Orosz, G.: Dynamics of connected vehicle systems with delayed acceleration feedback. Trans. Res. Part C **46**, 46–64 (2014)
6. Ge, J.I., Orosz, G.: Optimal control of connected vehicle systems with communication delay and driver reaction time. IEEE Trans. Intell. Trans. Syst. (2016) (published online). doi:10.1109/TITS.2016.2633164
7. Greenshields, B.D.: Studying traffic capacity by new methods. J. Appl. Psychol. **20**(3), 353–358 (1936)
8. Herman, R., Montroll, E.W., Potts, R.B., Rothery, R.W.: Traffic dynamics: analysis of stability in car following. Oper. Res. **7**(1), 86–106 (1959)
9. Insperger, T., Stépán, G.: Semi-Discretization for Time-Delay Systems: Stability and Engineering Applications. Applied Mathematical Sciences, vol. 178. Springer (2011)
10. Kesting, A., Treiber, M.: How reaction time, update time, and adaptation time influence the stability of traffic flow. Comput. Aided Civ. Infrastruct. Eng. **23**(2), 125–137 (2008)
11. Liang, C.Y., Peng, H.: Optimal adaptive cruise control with guaranteed string stability. Veh. Syst. Dyn. **32**(4–5), 313–330 (1999)
12. Öncü, S., Ploeg, J., van de Wouw, N., Nijmeijer, H.: Cooperative adaptive cruise control: network-aware analysis of string stability. IEEE Trans. Intell. Trans. Syst. **15**(4), 1527–1537 (2014)
13. Orosz, G.: Connected cruise control: modelling, delay effects, and nonlinear behaviour. Veh. Syst. Dyn. **54**(8), 1147–1176 (2016)
14. Orosz, G., Stépán, G.: Subcritical Hopf bifurcations in a car-following model with reaction-time delay. Proc. R. Soc. A **462**(2073), 2643–2670 (2006)

15. Orosz, G., Wilson, R.E., Stépán, G.: Traffic jams: dynamics and control. Philos. Trans. R. Soc. A **368**(1928), 4455–4479 (2010)
16. Qin, W.B., Gomez, M.M., Orosz, G.: Stability and frequency response under stochastic communication delays with applications to connected cruise control design. IEEE Trans. Intell. Trans. Syst. **18**(2), 388–403 (2017)
17. Stépán, G.: Retarded Dynamical Systems: Stability and Characteristic Functions, Pitman Research Notes in Mathematics, vol. 210. Longman (1989)
18. Swaroop, D., Hedrick, J.K.: String stability of interconnected systems. IEEE Trans. Autom. Control **41**(3), 349–357 (1996)
19. Swaroop, D., Hedrick, J.K., Chien, C.C., Ioannou, P.A.: A comparision of spacing and headway control laws for automatically controlled vehicles. Veh. Syst. Dyn. **23**(8), 597–625 (1994)
20. Wagner, P.: Fluid-dynamical and microscopic description of traffic flow - a data-driven comparison. Philos. Trans. R. Soc. A **368**(1928), 4481–4495 (2010)
21. Wang, M., Daamen, W., Hoogendoorn, S.P., van Arem, B.: Rolling horizon control framework for driver assistance systems. Part II: cooperative sensing and cooperative control. Trans. Res. Part C **40**, 290–311 (2014)
22. Zhang, L., Orosz, G.: Motif-based analysis of connected vehicle systems: delay effects and stability. IEEE Trans. Intell. Trans. Syst. **17**(6), 1638–1651 (2016)